A Retrofit Capacitive Sensing and Occupancy Detection System Using Fluorescent Lamps

John J. Cooley, *Student Member, IEEE,* Al-Thaddeus Avestruz, *Member, IEEE,* and Steven B.Leeb, *Fellow, IEEE*

Abstract—This paper presents a retrofit system that exploits a fluorescent lamp's own stray electric fields as an excitation source for capacitive sensing. The principal result of this work is the demonstration of sufficient sensitivity for detecting human occupants below the lamp. Experimental results are presented demonstrating detection ranges of 10 ft. between the lamp and the nearest edge of a human occupant. Theory is developed to inform system design choices and future work. A full-system simulation is presented including the simulation of a lumped element capacitive model. A circuit model of the fully-differential front end amplifier is developed and then validated as part of the full-system simulation.

Index Terms—Capacitive Sensing, Capacitive Model, Fluorescent Lamp, Fully-differential, SPICE, FastCap, Occupancy Sensing

I. INTRODUCTION

IN 2008, lighting consumed 0.72 Quadrillion Btu (QBtu) in the residential sector and 1.04 QBtu in the commercial sector [1]. This accounted for 15.3% and 22.6% of the total electricity delivered in the residential and commercial sectors, respectively [1]. The implications of technology that can significantly reduce energy consumed by lighting for national and even global energy challenges are obvious.

A. Context

This work is part of an on-going research effort to demonstrate a new low-cost retrofit sensor for extremely fine-grain control of lighting in energy management and other applications. Therefore, this work presents up to date developments in the context of previous work. Some basic theory was developed in [2] and [3]. Applications of the lamp sensor were discussed in [4]–[6]. Prior to this work, reference [6] presented the latest developments in our understanding of the lamp sensor operating principles and its feasibility as a demand-side energy management tool.

This work summarizes the modeling and system design approaches common to [4]–[6]. It extends the developments from previous work to include more fully-developed modeling concepts as well as new circuit analysis and circuit modeling, particularly with regard to the front-end amplifier. This work also includes a new full system simulation implemented in

SPICE and FastCap® and validated by comparison to experimental data. The full system simulation includes a lumped-element capacitive model of the system as well as a simulation of the signal conditioning electronics. Validating the simulated model simultaneously validates the capacitive model and the circuit model of the front-end amplifier presented here. For more detailed analysis and discussion, the reader may refer to [7].

B. Literature Review

The system presented here can be understood as a retrofit capacitive sensor for detecting human occupants. Similar work is demonstrated in reference [8], which presents a retrofit capacitive sensor for detecting occupants using in-place utility wiring. The system in [8] achieves detection ranges of about 1 m from the wire to the occupant. Reference [8] is one of many references that set a precedent for modeling a human as a conducting body. Other such precedents can be found in references [9]–[11].

Other applications of capacitive sensors include occupancy sensing in automobiles [11], fingerprint sensing [12], MEMS accelerometers and position sensors [13]–[15], pressure [16], humidity [17], and angular speed sensors [18], and a sensor for micro-fluids [19]. Capacitive sensors are also found in Medical applications [20], [21]. Other types of sensors are used for occupancy detection. For instance, reference [22] uses daylight MEMS sensors to inform a lighting energy management system. Pyorelectric Infrared (PIR) sensors are used for occupancy detection especially in demand-side energy management applications [23]–[25].

II. MODELING CONCEPTS

In order to configure the lamp and to design sensor electronics, it was helpful to first conceive simplifying abstractions of the system. The goal of this section is to review and develop the principles that support the particular type of simplification used here – the capacitive abstraction.

A. The Capacitive Abstraction and Quasistatic Limit

The operation of the sensor may be simplified by understanding the system in terms of quasi-electrostatic fields. Then, the system may be abstracted as a corresponding lumped-element capacitive model. The link between electrostatic field modeling and the capacitive abstraction can be examined by understanding the interactions between the electric fields
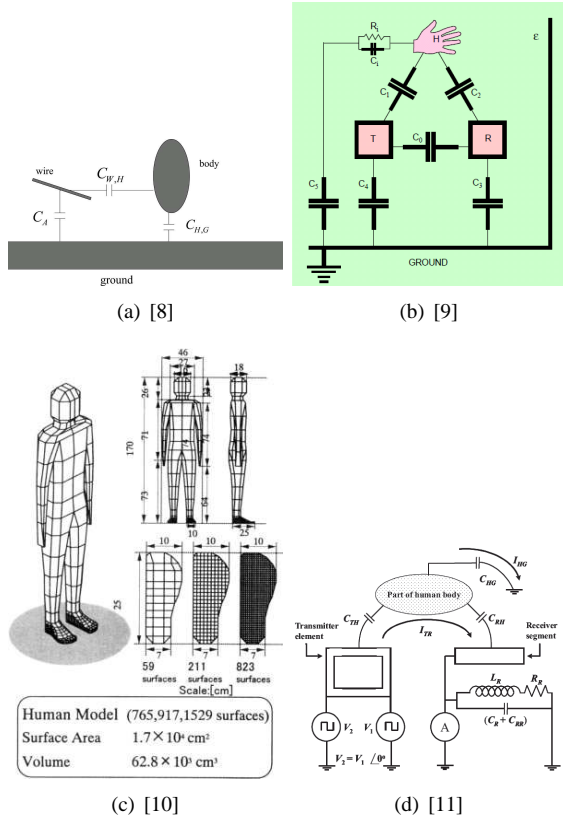
(a) [8]　　　(b) [9]

(c) [10]　　　(d) [11]

Fig. 1: Examples of systems with human conductor models taken from references [8]–[11].

and the conducting boundaries in the system. The boundary conditions that arise from Maxwell's equations are useful for studying these interactions:

$$\hat{n} \times \left(\vec{E}_1 - \vec{E}_2 \right) = 0. \tag{1}$$

$$\hat{n} \cdot \left(\vec{D}_1 - \vec{D}_2 \right) = \rho_s \tag{2}$$

Equation (1) says that tangential components of electric field strength are continuous and equation (2) says that the discontinuity in the electric flux normal to a boundary aries from the surface charge on that boundary. Combining the boundary condition in (1) with the fact that the electric field strength inside a conductor is forced to zero reveals that the tangential component of $\vec{E}$ at the surface of the conductor is zero. Therefore, the electric field must terminate normal to the (conducting) surface. Adding to this, the boundary condition on the electric flux density (2), reveals that the electric field at the surface is both normal to the surface *and* equal to the surface charge density divided by the permittivity of the medium around the conductor, i.e. $\vec{E} = \vec{E}_n = \frac{\rho_s}{\epsilon}$. The total charge in an area, A, on the surface of a conductor is therefore,

$$Q(t) = \iint_A \rho_s(t) dA$$
$$= \epsilon \iint_A \vec{E}_n(t) \cdot d\vec{A}$$
$$= \epsilon \Phi_e(t), \tag{3}$$

where $\Phi_e(t)$ is the total electric flux impinging normal to the surface with area A. If the electric field impinging on the surface of the conductor is the result of the potential on a second conductor, then the potential difference between any two points on those two conductors is

$$v_c(t) = \int_s \vec{E}(t) \cdot d\vec{s},$$

where (little) s is an arbitrary path between the two conductors. The voltage, $v_c(t)$, must be the potential difference between any points on those two conductors since they are both equipotential surfaces. Dividing the total charge on either conductor by this potential difference, by definition, yields the capacitance, i.e.

$$C \equiv \frac{\epsilon \iint_A \vec{E}_n(t) \cdot d\vec{A}}{\int_s \vec{E}(t) \cdot d\vec{s}} = \epsilon \frac{\Phi_e(t)}{v_c(t)}. \tag{4}$$

The current drawn onto a surface of area A, by an impinging electric field, $\vec{E}_n$, must be the time derivative of the total charge in that area. From (3), the current is then

$$\boxed{I(t) = \frac{\partial Q(t)}{\partial t} = \epsilon \frac{\partial \Phi_e(t)}{\partial t}} \tag{5}$$

and combining (4) with (5) reveals that

$$I(t) = C \frac{\partial v_c(t)}{\partial t}$$

as expected. Examining the expression in (5) reveals two key insights. First, the time-derivative of the electric flux must be nonzero to support a current on the conductor (electrode). Therefore, the electrical signal source must be time-varying and in most practical situations will be ac. Second, the time-derivative between the electric field and the current indicates a $90°$ phase shift for each sinusoidal component of excitation. A measurement electrode can therefore be thought of as a transducer between electric field and current. The transducer has a gain term proportional to the electrode area, A, the permittivity of the space containing the electric field, ϵ, and the frequency of the sinusoidal component of interest, ω. It also has a phase term equal to $90°$. Since the electric potential is always related to the electric field through a *spatial* not a time-derivative, that $90°$ phase shift occurs between the capacitor voltage and current as expected.

Implicit in the capacitive model abstraction is that the electric fields of interest vary slowly enough that the system is quasistatic. In a typical fluorescent lamp ballast, the excitation frequency ranges from 10 to 100 kHz. The corresponding free-space wavelength of light at say 50 kHz is $\lambda = c/f = 6$ km. Comparing that wavelength to the length-scales within the sensor system, e.g. between the lamp and the floor, or the height of a human occupant, reveals that the lamp sensor system is quasistatic for any reasonable ballast operating frequency.

The capacitive abstraction approach in this work generally attempts to lump conducting objects in the lamp sensor system as nodes in a circuit model. For instance, the backplane of the lamp, the measurement electrodes, and other large unmovable conducting objects in the detection field are taken as conduct-

2

ing nodes in the system. References [8]–[11] set precedents for treating a human as a conducting shell. Therefore, the human "target" is also taken as a conducting (and moving) node in the system.

B. Modeling the Floor

It is difficult to generalize the floor below the lamp as a conducting or a nonconducting plane. The correct treatment is perhaps dependent on the particular construction of any given floor. Moreover, if the floor is taken as a conducting plane, it must be determined if it is sufficiently well-connected to any reference potentials in the system, e.g. earth ground. Section V describes a method for controlling these ambiguities by iteratively comparing simulated results to experimental data. For now, the floor may simply be taken as another conducting node in the system.

C. Modeling the Source

Identifying a reasonable and useful model of the signal source is a key challenge in forming the lumped-element abstraction of the lamp sensor system. The signal source is derived from stray electric fields that couple from the ends and surfaces of the bulbs to the other conducting objects in the system. Lumping a single bulb into two pieces and comparing the resulting source impedance to the capacitive impedances that load it reveals that a voltage source (as opposed to a current source) representation is reasonable [2], [26]. Having chosen a voltage source representation, the two pieces of the lumped signal source model may be assigned corresponding (alternating) potentials.
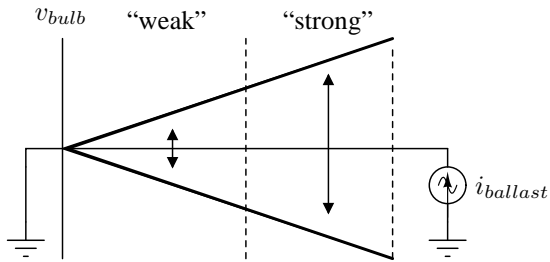

Fig. 2: Alternating linear voltage profile of a resistive bulb.

Figure 2 depicts the alternating linear voltage profile along the length of a driven resistive bulb. If the bulb is lumped into two halves, the half closer to the driven end may be called the "strong" half because the potentials in that piece vary a lot with respect to the undriven end (the ballast common). Then, the half closer to the undriven end may be called the "weak" half for obvious reasons. A corresponding lumped element model of a single driven fluorescent bulb is depicted in Figure 3. In Section V, a capacitive model is evaluated in which the signal source derived from a two-bulb lamp is represented using two lumped-element models like the one shown in Figure 3.

1) Signal Source Reference: In this electrostatic system, it is important to establish conceptions of the reference potentials and surfaces that support current return paths as we develop lumped-element models of the system. Because the signal

source itself is a conceived electrostatic model of driven fluorescent bulbs, the signal source reference potential and its physical location in the system is perhaps ambiguous. A convenient choice for the signal source reference is the ballast common shown as a ground symbol in Figure 3 because a) it is separated from the weak node in the bulb model by a relatively small (alternating) potential difference and b) it is a physical node in a the ballast circuit that allows for explicit ohmic connections. Therefore, in this work, the ballast common is called the "signal source reference" and those two node names are used interchangeably.
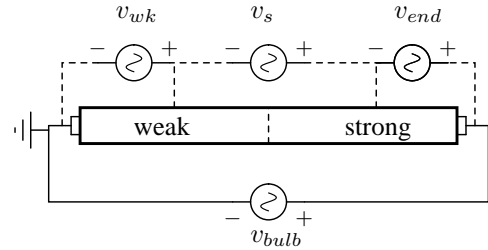

Fig. 3: Two bulb halves comprise the lumped element model of a single bulb.

D. Capacitive Models and Limitations

Having lumped all of the key elements in the system as conducting, and possibly driven nodes, the electric field behavior may be captured by considering the capacitive coupling between those nodes. Proceeding along these lines, a circuit model of the relatively complicated system can be drawn. The signal conditioning electronics can be taken to connect to that circuit at the electrode nodes and the system response can be determined by various means. An example of such a full system model is presented and evaluated in Section V using capacitance extraction software and a SPICE simulation.

Perhaps the primary limitation of the lumped element capacitive model originates in the modeling of the signal source. The electric field is related to the spatial derivative (gradient) of the corresponding scalar potential field, i.e. $\vec{E} = -\nabla\varphi$. When the bulb is lumped into two distinct halves and each half assigned a single potential, the variation of the actual potential along the length of those sections is neglected. Furthermore, abrupt changes are implicitly introduced in the potential at the ends of the bulb halves. The electric field corresponding to the lumped element model is inevitably an approximation of the actual electric field. Nonetheless, Section V will show that the approximations inherent to the lumped-element model allow for acceptable prediction of the system behavior.

III. LAMP SENSOR IMPLEMENTATION

The lamp sensor design incorporates two key system paradigms. First, the lamp is configured to support a "balanced" measurement of the electric fields. The signal conditioning electronics are fully-differential (FD) and are intended to take full advantage of the balanced source configuration. Second, the lamp sensor system is configured as a synchronous

detector. Synchronous detection achieves significant rejection of unwanted signal sources.

Figure 7 shows a simplified schematic of the implemented electronics. Typical passive component values are shown in Table I.

TABLE I: Typical system parameters and passive components.

Parameter	Value
$R_{f1,2}$	10 MΩ
$C_{f1,2}$	7.5 pF
R_{f3}	200 kΩ
C_{f3}	660 pF
R_{lim}	20 Ω
R_{pu}	500 Ω
R_{lpf}	10 kΩ
C_{lpf}	150 pF
f_{carr}	50 kHz

With the added costs of such systems in mind, the sensor electronics presented in this paper are intended to enable drop-in replacement of standard fluorescent lamp ballasts. The lamp sensor presented here requires two measurement electrodes positioned in front of the lamp. Those electrodes may be integrated into the lamp fixture or even sprayed onto the lamp cover using a translucent conductor like Indium-tin Oxide (ITO).
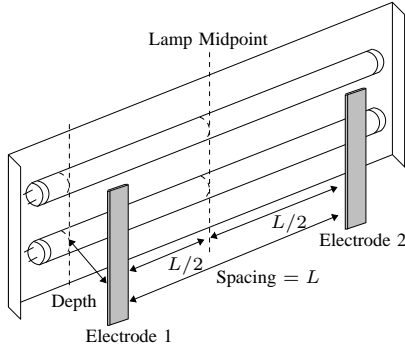
A. Lamp Configuration

Fig. 4: A diagram of the two-bulb fluorescent lamp and electrodes. The electrodes are spaced symmetrically about the center of the lamp.

In the experimental setup presented here, the lamp sensor is built upon a two-bulb lamp. A drawing of the lamp and measurement electrode configuration is shown in Figure 4. The electrodes in Figure 4 are used to measure the stray electric fields from the lamp. To create a balanced signal source, the ballast connections to one bulb in a two-bulb lamp are reversed as depicted in Figure 5. The resulting symmetry in the electric field can yield a "nulled" measurement when there is no target in the detection field. The front-end amplifier connected to the electrodes in this balanced configuration may have very high gain without saturating its output in the absence of a detection. Very small perturbations of the electric field may be detected as relatively large deviations from the null-point.
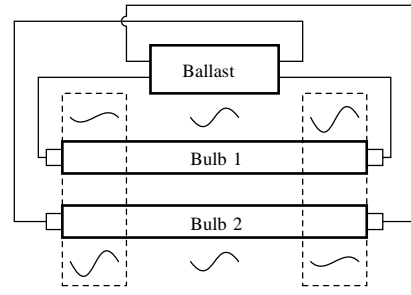

Fig. 5: Reversing the connections to one bulb in a two-bulb lamp yields the desired symmetry in the electric field source.
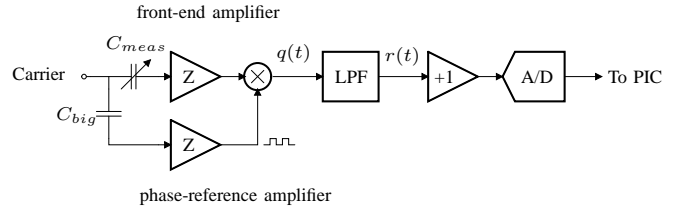
B. Synchronous Detection System

Fig. 6: A block diagram of the signal conditioning system. Transimpedance amplifiers are marked with a 'Z'.

Figure 6 shows a notional block diagram that highlights the synchronous detection scheme employed in the signal conditioning electronics. In the synchronous detection system, the carrier signal is the high-frequency alternating signal source driving the capacitive network below the lamp. Movement of the target into and within the detection field changes the amount of capacitive coupling from the lamp to the electrodes and thus the amount of current input to the front-end. This modulation effect is represented in Figure 6 with a variable capacitor, C_{meas}. A copy of the (unmodulated) carrier signal is fed forward and multiplied with the output of the front end amplifier. Multiplication by this phase reference achieves specificity in phase and frequency leading to a significant rejection of unwanted signals. A low-pass filter (LPF) attenuates the high-frequency residue after demodulation to yield the low-frequency modulations caused by the target below the lamp.

From reference [7], the output of such a synchronous detector, can be approximated as

$$r(t) = \frac{4}{\pi}\overline{Z_f}I_{id}(t)\cos\phi, \qquad (6)$$

in which $I_{id}(t)$ is the amplitude of the DM input current to the front-end, $\overline{Z_f}$ is the nominal frontend feedback impedance value and ϕ is the phase error between the front-end output and the phase reference.

C. Front-end Amplifier

The front-end amplifier is a fully-differential (FD) current-mode amplifier. It is designed to take advantage of the balanced signal source and to measure signals from the high-impedance capacitive system. Current-mode amplification is
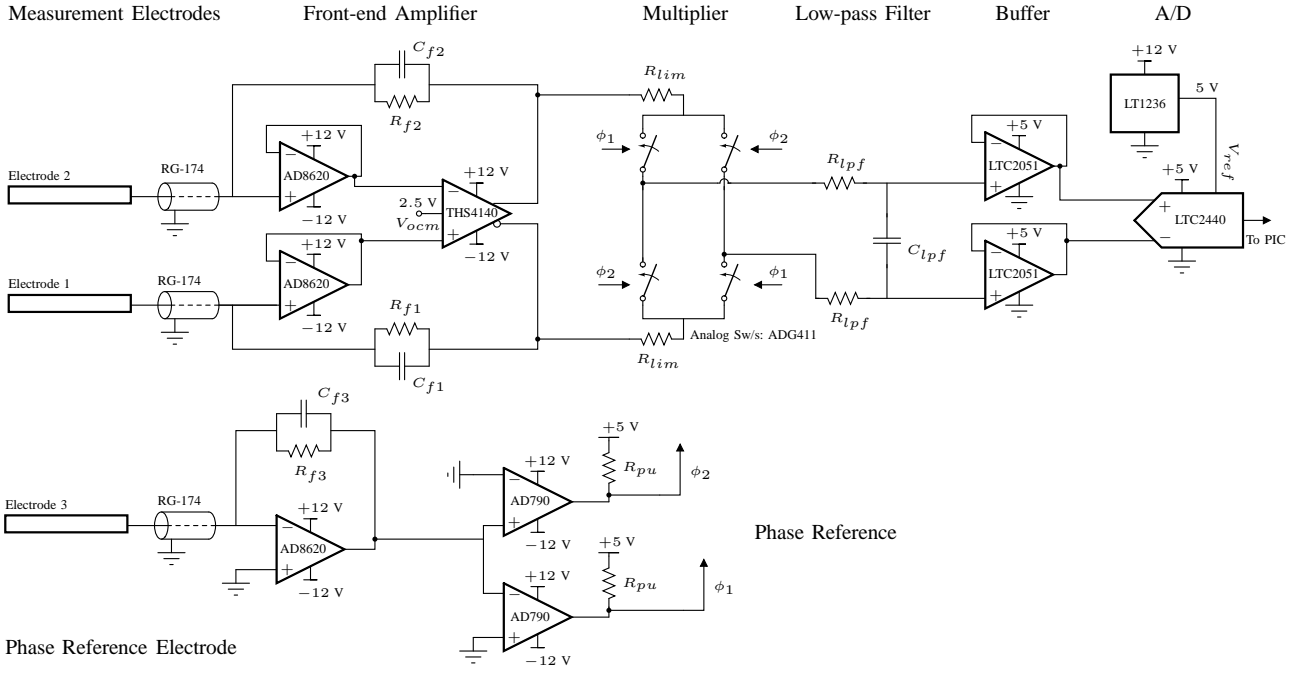
Fig. 7: A simplified schematic of the fully-differential signal conditioning electronics

implemented in Figure 7 with op-amps in closed-loop transimpedance configurations. Simply speaking, input currents see a small impedance or a "virtual short-circuit" between the input nodes of a transimpedance amplifier. This DM "virtual short-circuit" behavior is discussed in great detail in Reference [27]. The AD8620 op-amps shown in Figure 7 are configured as buffers. They were chosen for their JFET input devices, which draw very little input bias current and generate relatively little input-referred current noise. Having to supply very little input bias current allows for very large-valued feedback resistance, which is convenient when a large transimpedance is desired. The benefit of the low input-referred current noise of the JFET-input buffers is quantified in Section III-J.

1) Front-end Feedback Impedance Value Selection: Three main considerations led to the choice of feedback impedance components for the front-end amplifier. They were:

- Noise performance
- Closed-loop stability
- Phase-matching.

The transimpedance value should be large enough that the noise produced by the amplifier itself does not overwhelm amplified signals of interest. The value of the total impedance in the feedback network is equal to (half) of the nominal transimpedance for the FD front-end (see Section III-D). Therefore, either increasing $R_{f1,2}$ or decreasing $C_{f1,2}$ increases the transimpedance value. The values of the feedback impedance components themselves also influence the total amount of noise contributed by the front-end. Section III-J will show that noise embedded in the incoming signal currents dominates the total noise at the output of the sensor electronics implying that the implemented front-end is suitable in this regard. Because the JFET-input buffers (AD8620) require very little input bias current, a very large feedback resistor can be used. The

transimpedance value at ballast operating frequencies is then typically upper-bound by practical values for $C_{f1,2}$ and in that case, the transimpedance becomes capacitive.

The components that make up the transimpedance, $R_{f1,2}$ and $C_{f1,2}$, should also result in a stable closed-loop configuration. Section III-H derives the loop transfer function and evaluates the stability of an implemented sensor front-end. Finally, the transimpedance should be chosen so that the phase of the front-end output, with respect to the ac signal source, is well-matched to that of the phase reference amplifier. Section III-E shows that the implemented front-end amplifier achieves a calculated phase error of about $1°$ and a corresponding multiplicative error factor of about 0.99. Refer to Table I for typical front-end feedback component values.

### D. Front-end Amplifier Analytical Modeling

In reference [27], we analyze the FD transimpedance amplifier in Figure 8. Using a linear superposition approach, we show that the DM output voltage is

$$v_{od} =$$
$$\left(\frac{2\overline{Z_f}a_d - \frac{1}{2}a_c\Delta Z_f}{(1+a_d)} \right) i_{id} + \left(\frac{a_c\overline{Z_f} - a_d\Delta Z_f}{2(1+a_d)} \right) i_{ic}, \quad (7)$$

where i_{id} is the DM input current, i_{ic} is the CM input current, a_d is the op-amp DM-DM gain, a_c is the op-amp CM-DM gain. Average and difference impedances are defined as

$$\overline{Z_f} \equiv \frac{(Z_{f1} + Z_{f2})}{2}$$
$$\Delta Z_f \equiv Z_{f1} - Z_{f2}.$$

Examining the DM output voltage in (7), the term multiplying i_{id} is the DM transimpedance and describes the dominant behavior of the amplifier. For the perfectly ideal case, $a_d \rightarrow \infty$,

5
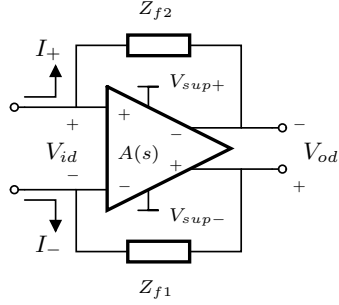
(a) A fully-differential transimpedance amplifier.
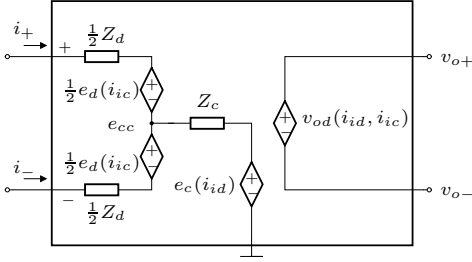
(b) A small-signal T-model [27].

Fig. 8: A fully-differential transimpedance amplifier and a small-signal model from [27].

$a_c \to 0$, and $\Delta Z_f \to 0\Omega$, the "fully-ideal" output voltage becomes

$$v_{od} = 2\overline{Z_f}i_{id}.$$ (8)

A similar analysis leads to expressions for the CM and DM input voltages:

$$v_{ic} = -i_{id}\frac{\Delta Z_f}{2} + i_{ic}\frac{\overline{Z_f}}{2}$$ (9)

and

$$v_{id} = i_{id}\left(\frac{2\overline{Z_f} + \frac{1}{2}\Delta Z_f a_c}{(1 + a_d)}\right) - i_{ic}\left(\frac{\Delta Z_f + \overline{Z_f}a_c}{2(1 + a_d)}\right).$$ (10)

Based on the analytical results in (7)-(10), we form approximate circuit models of the transimpedance amplifier shown in Figure 8(b) using the model parameters:

$$Z_c = \left(\frac{\overline{Z_f}}{2}\right)$$ (11)

$$Z_d = \left(\frac{2\overline{Z_f} + \frac{1}{2}\Delta Z_f a_c}{(1 + a_d)}\right)$$ (12)

$$e_c(i_{id}) = -i_{id}\left(\frac{\Delta Z_f}{2}\right)$$ (13)

$$e_d(i_{ic}) = i_{ic}\left(-\frac{\Delta Z_f}{2(1 + a_d)} - \frac{\overline{Z_f}a_c}{2(1 + a_d)}\right).$$ (14)

This model of the front-end is validated as part of the simulation in Section V.

E. Phase-Reference Amplifier

The phase reference is measured with a single-ended transimpedance amplifier that is capacitively-coupled to the bulbs similar to the front-end amplifier. The phase reference electrode can be taped to the bulb or to the ballast wire. It can also be built into the ballast as a trace adjacent to the drive signal for the bulb or as an explicit capacitor coupling to the ballast drive signal. The output of the phase reference amplifier drives opposite inputs of two comparitors in order to generate two (barred and unbarred) control signals for the FD multiplier.

1) Phase-Reference Feedback Impedance Value Selection: Three main considerations led to the choice of feedback impedance components for the phase-reference amplifier. They were:

- Output Signal level
- Closed-loop stability
- Phase-matching.

The transimpedance value for the phase reference amplifier should be chosen so that, given the configuration of the phase reference electrode, the amplifier's output signal is well-behaved. That is, the output signal should be large enough to support good transitions in the comparators, but it should not saturate the output of the phase reference amplifier. Depending on the particular implementation of the phase reference electrode, the transimpedance value that satisfies this criterion is most easily found by experimentation. Stability considerations for choosing the transimpedance for the phase reference amplifier are addressed in Section III-H.

The phase-reference amplifier's output should be well-matched in phase to the output of the front-end amplifier. From Section III-D, the closed-loop frequency response of the FD transimpedance amplifier can be approximated with the transimpedance, $2\overline{Z_f}$. Similarly, the closed-loop response of the SE amplifier can be approximated by its feedback impedance value. Given the typical passive component values from Table I the magnitude and phase of the closed-loop response for the phase-reference amplifier is

$$|Z_{f3}| = 4.82 \text{ k}\Omega$$
$$\angle Z_{f3} = -88.6°$$ (15)

and for the front-end amplifier,

$$|2\overline{Z_f}| = 424 \text{ k}\Omega$$
$$\angle 2\overline{Z_f} = -87.6°.$$ (16)

Equations (15) and (16) show a phase error of $\phi = 1°$ between the front-end and phase-reference amplifiers' closed-loop response at f_c. From equation (6), the multiplicative error factor corresponding to this phase error is

$$\eta = \cos\phi = \cos 1° \approx 0.99985.$$ (17)

Because both the front-end and the phase-reference amplifiers are capacitively coupled to the signal source and because η is close to unity, the outputs of the two amplifiers should be well-matched in phase. Equations (15) and (16) also reveal that both transimpedances are largely capacitive at the signal frequency, f_c. Therefore, the phase between the *signal source*

voltage originating in the lamp and the outputs of the two amplifiers should be nearly $0°$.[1] Refer to Table I for typical phase-reference feedback component values.

F. Electrode Cable Shields

In this implementation of the lamp sensor, the electrodes are connected to the input nodes of the amplifiers with shielded coaxial cables connected to the lamp sensor power supply ground as shown in Figure 7. Those shields reduce coupling to the wires between the electrodes and the electronics. However, they also present a significant capacitance between the input nodes and power supply ground. That shield capacitance has different implications depending on the configuration of the lamp sensor system. For instance, if the power supply ground is well-connected or even coupled to the signal source reference, those shields may actually shunt some of the desired signal currents away from the amplifier. On the other hand, if the power supply ground and signal source reference are not well-connected, the shield capacitances should have a lesser impact on desired signal currents. In either case, the shield capacitances should be taken into account when enumerating the stray input capacitances at the input nodes of the amplifiers.

G. Stray Input Capacitances

There are some significant capacitances between the amplifier input nodes and power supply or incremental ground in the implementation of the lamp sensor presented here. These "stray input capacitances" largely consist of the coaxial shield capacitance from the electrode cables, the stray capacitance between PCB traces and the input capacitance of the AD8620 op-amps in the front-end amplifier. The total stray input capacitance was measured, using an LCR meter operating at 50 kHz, between the input node on the lamp sensor PCB connected to electrode 1 in Figure 7 and the lamp sensor's power supply ground.[2] For this measurement, the lamp sensor was powered off and the feedback passive components, R_{f1} and C_{f1}, were removed from the PCB. An electrode with a 36-inch `RG-174` electrode cable was attached to the input node of interest.

For the analysis and modeling in the rest of this work, the total stray capacitance is taken to be that measured for one particular PCB:

$$\boxed{C_{stray} = 159 \text{ pF}}. \tag{18}$$

For convenience, the stray input capacitances were assumed to be the same for both input nodes of the front-end amplifier and for the input node of the phase-reference amplifier.

H. Feedback Compensation

Closed-loop stability is readily evaluated by analyzing the open-loop transfer functions ("loop transfer functions"). Analysis of the front-end amplifier shown in Figure 7 leads to the following loop-transfer function [7]:

$$\boxed{L(s) = a_d(s)H_J(s)\frac{Z}{Z + Z_f}}, \tag{19}$$

where $H_J(s)$ is the closed-loop transfer function of the JFET-input buffer op-amps (AD8620), $a_d(s)$ is the DM gain of the THS4140 op-amp, Z is the nominal impedance between the op-amp inputs and incremental ground, and Z_f is the nominal feedback impedance. A similar analysis leads to the loop transfer function for the (single-ended) phase-reference amplifier [7]:

$$\boxed{L_p(s) = a_J(s)\frac{Z}{Z + Z_{f3}}}, \tag{20}$$

in which $a_J(s)$ is the DM voltage gain of the AD8620 op-amp, Z is the impedance between the op-amp inverting input and incremental ground and Z_{f3} is the value of the amplifier's feedback impedance. Stray input capacitances from Section III-G comprise Z in (19) and (20).

(a) Front-end, P.M. $= 75.9°$

(b) Phase-reference, P.M. $= 90°$

Fig. 9: Open-loop frequency responses showing suitable phase margin.

---

[1] or 180° depending on the implementation, e.g. inverting or non-inverting amplification.
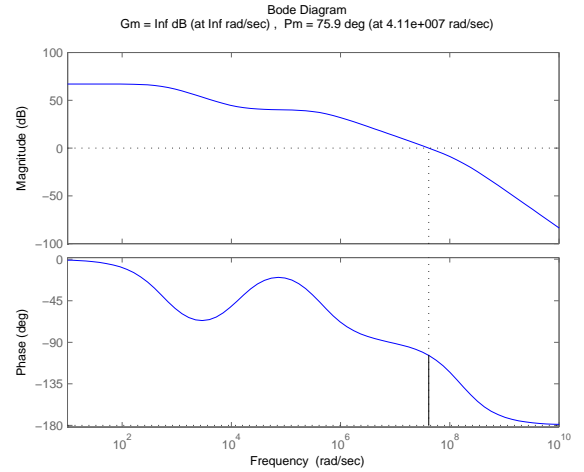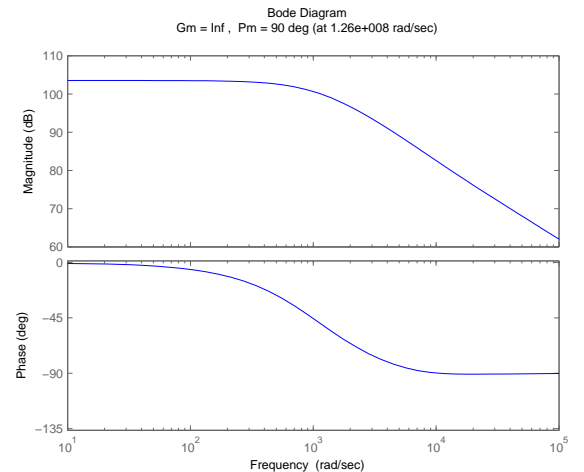
[2] Either input node yielded about the same capacitance.

To evaluate the stability of both amplifiers, dominant pole models of the op-amp dynamics were extracted from the datasheets [28], [29]. Those model parameters are shown in Table II. Finally, feedback impedances in this implementation

TABLE II: Dominant Pole Models

Part	Parameter	Value
THS4140	GBW	2,238.7 Hz
[29]	Dominant Pole	67 kHz
AD8620	GBW	150 kHz
[28]	Dominant Pole	166 Hz

were those shown in Table I. Bode plots of the loop transfer functions are shown in Figure 9. Both plots show good phase margin indicating suitable stability.

Closer examination of the loop-transfer functions reveals the manner in which the feedback compensation achieves closed-loop stability. The loop-transfer, $L(s)$, for the front-end can be re-written as

$$L(s) = a_d(s)H_J(s)\left(\frac{1+R_fsC_f}{1+R_fs(C_{in}+C_f)}\right), \qquad (21)$$

where C_{in} is the total capacitance from the either input node to ground. With the dominant pole models, the gain terms $a_d(s)$ and $H_J(s)$ each contribute one pole but no zeros. The addition of R_f contributes one additional pole and the addition of C_f contributes one additional zero (consider equation (21) for $C_f = 0$). The additional zero in the vicinity of at least one of the poles significantly reduces the phase of the loop transfer function near cross-over, thereby increasing the phase margin of the system. The incorporation of the parallel capacitance, C_f, in the feedback network is a form of lead compensation because it adds leading phase shift or positive phase to the output signal relative to the input signal at all frequencies [30].

I. Fully-differential Synchronous Detector

The electronics between the front-end and the A/D are fully-differential (FD) primarily because this eliminates the need for a differential-to-single-ended converter. The FD signal chain also rejects CM pickup and power-supply disturbances.

The FD multiplier is implemented with a full-bridge of analog switches controlled according to the measured phase reference signal. The FD low-pass filter is implemented as an R-C ladder and serves to attenuate the high-frequency residue left after demodulation. Because band-limiting effects in the final A/D are significant, the LPF may be viewed as an anti-aliasing filter while the majority of interpolation occurs in the A/D itself. A typical sampling rate for the A/D is 14 sps. Taking the corresponding Nyquist rate (7 Hz) as the low-pass bandwidth, the synchronous detector will largely reject unwanted signals whose frequency differs from that of the desired signal by more than 7 Hz. Given typical carrier frequencies near 50 kHz, the synchronous detector effectively achieves extremely aggressive bandlimiting of the incoming modulated signal.

Two chopper-stabilized op-amps buffer the output of the LPF. Those buffers present a high input impedance to the preceding LPF and a low-output impedance to the ensuing A/D.

Therefore, inserting those buffers de-couples the frequency response design constraints of the LPF from the maximum source impedance constraints specified for the A/D [31].

J. Noise

The electronics were designed to contribute less noise to the final output than the noise inherent in the measured signal. To evaluate our efforts in this regard, the noise contributions from the implemented electronics may be enumerated analytically. Because the noise inherent in the measured signal is most easily quantified empirically, experimental data ultimately verified the low-noise design. From reference [7], the total noise voltage contribution of the front-end amplifier at the A/D input (the output of the synchronous detector) is

$$v_{n,amp} \approx \frac{2}{\pi}\sqrt{BW_n} \times$$
$$\sqrt{\left((e_{nT}^2 + 2e_{nJ}^2)\left(\frac{Z_f}{Z}\right)_{\omega_c}^2 + \left(2i_{nJ}^2 + 2\frac{4kT}{R_f}\right)Z_f|_{\omega_c}^2\right)} \text{V}_{rms},$$
$$(22)$$

in which Z is comprised of the stray input capacitances from Section III-G and the complex impedances may be taken as their values at the carrier frequency because the synchronous detector output is narrowband [7]. Also e_{nT} and e_{nJ} are the input-referred voltage noises for the THS4140 and AD8620 parts, respectively, i_{nJ} is the input-referred current noise of the AD8620 part, k is the Boltzmann constant, T is temperature, R_f is the nominal feedback resistance in the front-end, and ω_c is the carrier or ballast operating frequency. Finally, BW_n is the noise bandwidth and is ultimately constrained by the A/D to be 12.4 Hz for a typical sampling rate of 14 sps. Using equation (22), the passive component values in Table I, the datasheets for the parts in Figure 7, the noise sources at the input to the A/D may be enumerated as follows [7]:[3]

$$v_{n,amp} = 500 \text{ nV}_{rms}$$
$$v_{n,buff} = 1.5 \text{ }\mu\text{V}_{p-p}, \text{ typical in } 0.1 - 10 \text{ Hz}$$
$$v_{n,AD} = 250 \text{ nV}_{rms}. \qquad (23)$$

From (23), the dominant noise source originates in the buffers that precede the A/D inputs. Therefore, the front-end is suitably low-noise in the sense that it is *not* the dominant noise source. Whether or not the electronics as a whole are suitably low-noise depends on the noise content inherent in the measured signals. Time-domain plots of typical noise at the lamp sensor output are shown in Figure 10. Comparing the noise in Figure 10(a) to that in Figure 10(b) reveals that the signal conditioning electronics contribute negligibly to the overall noise content. Therefore, the signal conditioning electronics are suitably low-noise.

IV. RANGE TEST

To evaluate the sensitivity of the implemented lamp sensor, a range test was performed. A cart-mounted system, shown in Figure 11, was constructed to collect sensitivity data.

---

[3]and assuming an ambient temperature of 300 K

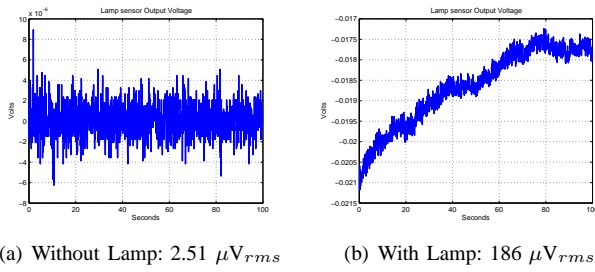(a) Without Lamp: 2.51 μV_{rms} (b) With Lamp: 186 μV_{rms}

Fig. 10: Noise Data: values are average noise levels in a 10-sec window.

Examples of the output voltage data collected from the cart-mounted lamp sensor during the range test are shown in Figure 12. Experimental setup parameters including passive component values for the sensor are shown in Table III.


Fig. 11: A photograph of the cart-mounted lamp experimental setup

Data was taken for 20 different electrode configurations. Each configuration consisted of an electrode spacing and depth as defined in Figure 4. Each sample consisted of one pass of a human target walking in front of the horizontally mounted lamp. The metric for each sample was the ac rms output voltage, $V_{ac,rms}$. For each configuration, 10 control samples (noise floor measurements) were taken with no target. Then, for each range in each electrode configuration, 5 samples were taken with a target passing in front of the lamp. A Z-test in MATLAB® was performed on the data comparing each 5-sample data set for each range to the control data set for the corresponding electrode configuration. In our detection rule, the sample data sets had to demonstrate a mean $V_{ac,rms}$ larger than that of the control data sets with a confidence level of 99% or better. The resulting statistical data are shown in Table IV at the boundary of the detection range. The range varies along the columns. The electrode configuration varies along the rows. The data in Table IV indicate detection ranges of 7-10 ft., depending on the electrode configuration.

V. CAPACITIVE MODEL AND SIMULATION

This section presents and evaluates a SPICE model of the lamp sensor system including a lumped element capacitive
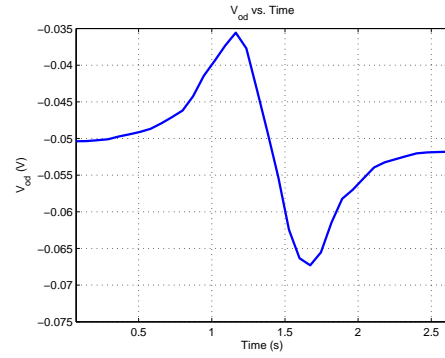
(a) 4 ft.
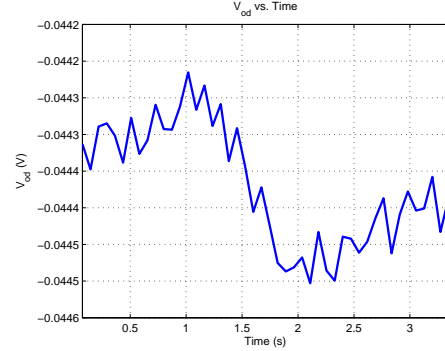
(b) 10 ft.

Fig. 12: Example output data plots taken from the range test for a passing target. (Configuration 44x5)

TABLE III: Range Test Experimental Setup Parameters.

Parameter	Note / Value
$R_{f1,2}$	1 MΩ
$C_{f1,2}$	1 pF
R_{f3}	80 kΩ
C_{f3}	30 pF
f_{carr}	42 kHz
Phase Ref Elect.	Taped to bulb center
Earth, gnd, Common	Not explicitly connected

model. A depiction of the model implemented in LTspice® is shown in Figure 18.

A. SPICE Model

The SPICE simulation (Figure 18) includes a lumped element capacitive model like the one described in Section II, a circuit model of the front-end amplifier taken from Section III-D, and a model of the entire signal processing chain described in Section III. The netlist for the front-end amplifier can be found in Appendix A. The remaining SPICE parameters can be found in Appendix B. With these components, the output voltage of the synchronous detector, corresponding to equation (6), can be read directly from the simulated results.

1) Phase Accounting: By accounting for the phase contributions in SPICE, the simulation is expected to yield the correct polarity of the output voltage. The phase reference in the SPICE simulation includes an additional 270° phase lag

9

TABLE IV: Detection Data $p-values$ for Various Electrode Configurations at the Limit of the Detection Range.

Spacing(in.)	Depth(in.)	p-values 7ft.	8ft.	9ft.	10ft.	11ft.	Noise Floor ($\mu V_{ac,rms}$)
44	5	0	0	0	2.53×10^{-4}	0.328	54.5
	4	0	0	4.63×10^{-7}	0.0165	N/A	65.1
	3	0	0	0	4.85×10^{-6}	0.661	98.9
	2	0	$<10^{-7}$	0.0426	N/A	N/A	168.5
38	5	0	0	3.05×10^{-5}	0.0240	N/A	61.8
	4	0	0	4.93×10^{-5}	0.865	N/A	67.3
	3	0	0	$<10^{-7}$	0.133	N/A	62.7
	2	0	0	0.00200	0.0160	N/A	74.0
28	5	0	0	0	$<10^{-7}$	0.306	45.2
	4	0	0	1.19×10^{-4}	0.676	N/A	70.7
	3	0	0	$<10^{-7}$	0.884	N/A	52.3
	2	0	2.62×10^{-5}	0.00100	0.0270	N/A	65.3
19	5	0	$<10^{-7}$	0.382	N/A	N/A	55.4
	4	0	0	$<10^{-7}$	0.126	N/A	41.6
	3	0	$<10^{-7}$	0.0120	N/A	N/A	45.4
	2	0	0	1.01×10^{-5}	0.0340	N/A	42.2
15	5	0	$<10^{-7}$	0.0360	N/A	N/A	40.9
	4	$<10^{-7}$	0.0210	N/A	N/A	N/A	51.5
	3	0	$<10^{-7}$	0.0640	N/A	N/A	49.9
	2	$<10^{-7}$	0.0120	N/A	N/A	N/A	57.2

to account for the inversion in the phase reference amplifier and the $90°$ phase contribution from the front-end amplifier, not accounted for by the front-end SPICE circuit model.[4] The ADG411 analog switches shown in Figure 7 are active-low. This was accounted for in the SPICE simulation by controlling the simulated switches with logically-inverted ("barred") versions of the control signals from the comparators.

B. Capacitive Model

The intent of the capacitive modeling approach in this section is to build the model by considering all of the capacitances between all of the conducting nodes in the system. Each conducting node is initially taken to be floating. Depending on the configuration of the system or on measurements taken from the experimental setup, some of those nodes may then be modeled as being to a particular potential.

1) FastCap® - Capacitance Extraction: A capacitance extraction software, FastCap®, was used to determine the lumped element capacitance values to insert into the SPICE simulation [32]. A screenshot of the 3D model built for this purpose is shown in Figure 13. In the 3D model, one can see the floor at the bottom, the human target on the left and the fluorsecent lamp and electrodes (lamp sensor) above the center of the floor. Also included in the model are other unmovable conducting objects such as a large cabinet on the left, as well as overhead pipes, other lamps, a large duct and a power strip case that appears at waist level.

For each simulation, FastCap® generated an output matrix like the one shown in Figure 14. The output matrices contained the values of the capacitances between each conductor in the system. For instance, the matrix element at row 5, column 8, corresponded to the net capacitance between conductor 5 (the left electrode) and conductor 8 (the target).[5]

[4]The $90°$ phase contribution is due to the capacitive feedback elements in the real sensor front end. For simplicity, in the SPICE model, we take the entire feedback network to be purely real with a resistance equal to the magnitude of the impedance of the actual feedback network.

[5]According to the Maxwell capacitance matrix format, mutual capacitances (off-diagonal elements) are reported as the negative of their actual value while diagonal elements are reported as positive values. If the capacitance matrix has non-negative off diagonals, we expect that there has been a problem with the extraction of the capacitance values [32].

Typical simulated capacitances are shown in Table V. Those capacitances represent the simulation of the target under the left edge of the lamp in Figure 13 with the lamp at a height of 2.43 m. Several capacitances in simulation are taken to be fixed as the target moves under the lamp ("Assumed Fixed") while only a few are taken to vary while the target moves ("Vary with Target"). When the target passes directly below the center of the lamp, many capacitances can also be assumed from symmetry.

TABLE V: Typical Simulated Capacitances (shown for a target positioned under the left end of the lamp sensor depicted in Figures 13 and 16(a)).

Capacitance	Value	Notes
		Vary with Target
L. strong-Target	300 fF	
R. strong-Target	167 fF	
L. Electrode-Target	534 fF	
R. Electrode-Target	187 fF	
Backplane-Target	14.3 pF	
Cabinet-Target	2.5 pF	
		Assumed Fixed
L. strong-L. Electrode	477 fF	
L. strong-L. weak	126 fF	
L. strong-R. strong	41 fF	
L. strong-Cabinet	56 fF	
R. strong-Cabinet	62 fF	
L. weak-Cabinet	81 fF	
R. weak-Cabinet	53 fF	
L. Electrode-Cabinet	102 fF	
R. Electrode-Cabinet	52 fF	
Backplane-Cabinet	19 pF	
L. strong-R. Electrode	27 fF	
L. strong-Backplane	3 pF	
L. Electrode-Backplane	3.1 pF	
L. strong-R. weak	1.6 pF	
Floor-Backplane	79.7 pF	
Floor-Cabinet	121 pF	
Floor-L. strong	321 fF	
Floor-L. Electrode	401 fF	
Floor-Target	42.4 pF	"Shoe Capacitance"

2) Simulating the Floor: Section II, discussed the ambiguity concerning the correct model of the floor below the lamp. The floor in the experimental setup was a tile floor on top of a concrete slab of unknown construction. Two key questions arise: 1) is the floor is well-represented by a conducting plane? and 2) if it is well-represented by a conducting plane, is it
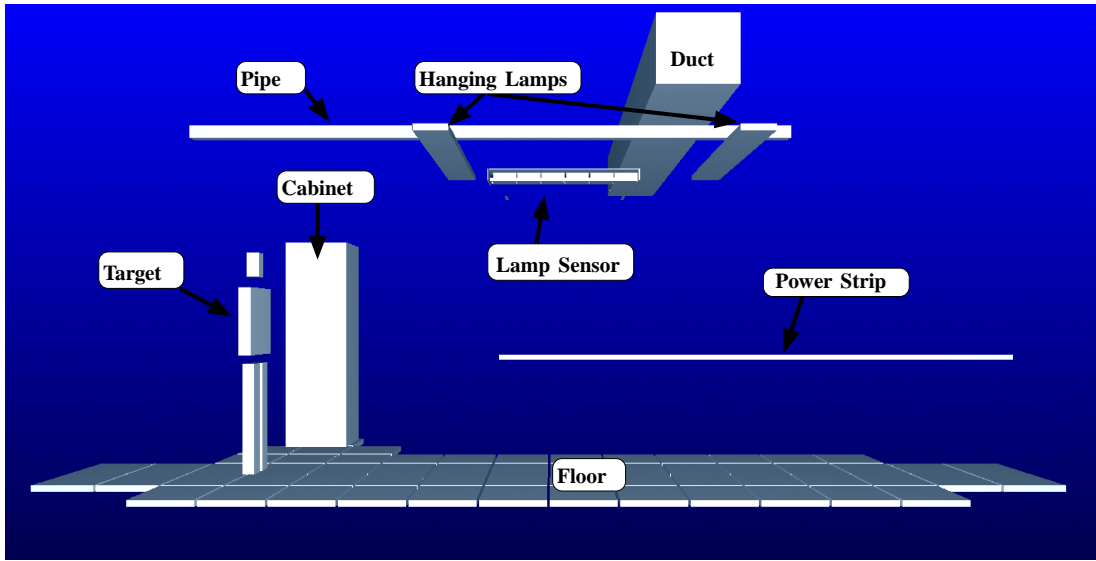
Fig. 13: A screenshot of the FastCap® 3D model

```
CAPACITANCE MATRIX, femtofarads
                   1          2          3          4          5          6          7          8          9         10
1%GROUP1   1 3.295e+004      -39.1     -122.9      -1623     -470.8     -25.47 -2.993e+004     -299.7     -39.45     -221.7
1%GROUP2   2      -39.1 3.304e+004      -1617     -126.5     -25.68     -455.5 -3.021e+004     -167.4      -56.4     -209.2
1%GROUP3   3     -122.9      -1617 3.296e+004     -39.19     -469.7     -24.75 -3.002e+004     -291.4     -65.85       -179
1%GROUP4   4      -1623     -126.5     -39.19 3.302e+004     -26.19     -456.3 -3.011e+004     -175.5     -47.29     -252.8
1%GROUP5   5     -470.8     -25.68     -469.7     -26.19       4860     -15.86      -2861     -536.9     -74.87       -224
1%GROUP6   6     -25.47     -455.5     -24.75     -456.3     -15.86       4843      -3127     -187.2     -43.94     -328.7
1%GROUP7   7 -2.993e+004 -3.021e+004 -3.002e+004 -3.011e+004      -2861      -3127 3.479e+005 -1.43e+004 -1.906e+004   -7.6e+004
1%GROUP8   8     -299.7     -167.4     -291.4     -175.5     -536.9     -187.2 -1.43e+004 6.776e+004      -2511 -4.538e+004
1%GROUP9   9     -39.45      -56.4     -65.85     -47.29     -74.87     -43.94 -1.906e+004      -2511 1.656e+005 -1.227e+005
1%GROUP10 10     -221.7     -209.2       -179     -252.8       -224     -328.7  -7.6e+004 -4.538e+004 -1.227e+005 3.633e+005
```

Fig. 14: An example FastCap® output matrix

well-connected to reference potentials in the system, e.g. earth ground? To control these ambiguities, data from simulation was compared to data from the experimental system with and without an artificial conducting floor made of Aluminum foil. The artificial conducting floor was also connected and disconnected to or from the earth ground reference. Because little change was observed in the measured output from the experimental system among the three cases, it was speculated that the actual floor below the lamp was well-represented by an earthed conducting plane. In the SPICE model of Figure 18, this was implemented as a short circuit between the "earth" and "floor" nodes. In the FastCap® 3D model of Figure 13, this is manifested as a conducting plane below the lamp and the target.[6]

Having a conducting plane model of the floor, the effective depth of that conducting floor ("effective conducting floor depth") was also adjusted by comparing simulated and experimental data. To that end, a conducting plane was positioned in the FastCap® simulation some distance below the surface of the actual floor. That distance was determined empirically, by closely matching the peak deviation of simulated data

[6]Segmenting the floor plane into smaller panels, as shown in Figure 13, aided the FastCap simulator. In general, this method of breaking the conductors into pieces aided the simulation and was a practical necessity for getting the simulator to work properly. Common results yielded by a model without enough of this kind of granularity included "non-negative off-diagonals" and "failure to converge" errors as well as prohibitively long computation times.
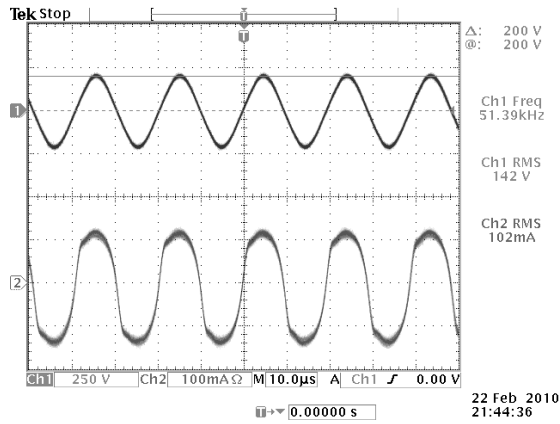
taken from the SPICE simulation to the peak deviation of corresponding experimental data. The effective conducting floor depth was set using data with the lamp set at a height of 2.43 m and then held fixed for the other experiments. The final value of the effective conducting floor depth is shown in Table VI.

3) Simulating the Source: The capacitive model in Figure 18 includes a model of the signal source consistent with the developments in Section II. That is, in the signal source model, each bulb consists of two nodes - "strong" and "weak". Because the model in Section II divides the bulb into two distinct pieces, it is necessary to assign each piece an alternating potential with respect to the signal source reference. Based on the alternating linear voltage profile of a single (resistive) bulb shown in Figure 2, it is convenient to assign the model parameters for the signal source model in Figure 3 as follows:

$$v_{wk} = \frac{1}{4}v_{bulb}, \ v_s = \frac{1}{2}v_{bulb}, \ v_{end} = \frac{1}{4}v_{bulb}, \quad (24)$$

where the total bulb voltage is comprised of the three voltages, i.e.

$$v_{bulb} = v_{wk} + v_s + v_{end}. \quad (25)$$

Figure 15 shows an oscilloscope shot of the bulb voltage and current under the experimental conditions. It shows a bulb voltage amplitude of 200 V and an operating frequency of about 50 kHz. With $v_{bulb} = 200$ V, the pieces of the signal

Fig. 15: Fluorescent bulb voltage (top) and current (bottom).

source model become

$$v_{wk} = 50 \text{ V} \tag{26}$$

$$v_s = 100 \text{ V} \tag{27}$$

$$v_{end} = 50 \text{ V}. \tag{28}$$

The signal source model parameters are summarized in Table VI.

Note that the polarity and lack of phase shift between the measured bulb voltage and current validates the assumption that the bulb is well-modeled at high-frequency as a resistor. The bulb voltage and current in Figure 15 indicate a bulb resistance of approximately 1 kΩ.

C. Connecting "Earth," "GND," and "Common"

In the lamp sensor system, there are several "reference potentials" including the lamp sensor power supply ground ("gnd"), the ballast common ("common"), and earth ground ("earth").[7] To simplify the simulation, all of those reference potentials were explicitly shorted together in both the experimental setup and in simulation (see the bottom left of Figure 18).[8]

Certain conductors were found to be connected to the reference potentials. It was verified with an ohm meter (and a piece of sandpaper) that the pipes, fluorescent lamp backplanes, duct and power strip case were earthed. Those corresponding nodes in Figure 18 were shorted to earth. On the other hand, the cabinet was not connected to earth and was therefore modeled in Figure 18 as a floating node.

Some of the capacitances in Table V do not effect the simulated results depending on the connections between reference potentials. For instance, the capacitance between the backplane and the floor is irrelevant when both the backplane and the floor are taken to be connected to earth.

D. Simulation Procedure

The simulation was conducted using the FastCap® model in Figure 13. The simulated capacitances were inserted into

[7]In the LTSPICE simulation, the triangular ground symbol is equivalent to any node labeled "gnd."

[8]Shorting the ballast common to earth required that the L/N utility feed to the ballast be isolated.

the SPICE model shown in Figure 18 and the simulated lamp sensor output voltage was read directly from SPICE.

First, the fixed capacitances listed as "assumed fixed" in Table V were taken from a FastCap® simulation with the target below the left end of the lamp. Then, the simulated offset was measured by inserting all of the capacitances from that FastCap® simulation into the SPICE model of Figure 18 and reducing the "vary with target" capacitances by 10 orders of magnitude. The resulting output voltage was saved so that it could be subtracted from the rest of the simulated output values.

Finally, thirty seven separate simulations like the one depicted in Figure 13 were used to model a passing occupant. For each simulation, the target was moved, in 20 cm increments, along the path that the real target in the experimental setup would take. In the simulation, the left end of the lamp was positioned at the x-origin (x = 0 m). The target started 3 m to the left of the origin in simulation (x = -3.0 m) and was stopped 3 m beyond the right end of the lamp (x = 4.2 m). The final output plots re-center the data so that $x = 0$ corresponds to the center of the lamp. Simulation parameters are summarized in Table VI. An example list (.lst) file for creating the model in Figure 13 can be found in Appendix C.

TABLE VI: Simulation Parameters.

| Simulation Parameter	Note / Value	Source
$v_{bulb1,2}$	200 V	Oscilloscope (Figure 15)
$v_{s1,2}$	100 V	Model (Section II)
$v_{wk1,2}$	50 V	Model (Section II)
f_c	50 kHz	Oscilloscope (Figure 15)
$Z_{f1,2}$	423 kΩ	Calculated as $|Z_f|$ @ $\omega = 2\pi f_c$
Earth, gnd, Common	Explicitly connected	N/A
Electrode Depth	14.5 cm	Meas'd between electrodes and bulb surface
Electrode Spacing	98 cm	Measured between electrodes
Lamp Height	2.28, 2.43, 2.58 m	Measured from bulb surface to floor
Target Height	1.83 m	Measured height of human occupant
Effective Conducting Floor Depth	-2.5 cm	Empirical (Section V-B2)

E. Experimental Procedure

Experimental data was taken from the experimental setup shown in Figure 16(a). The photograph in Figure 16(a) is labeled so that it is obvious how the experimental setup corresponds to the 3D model shown in Figure 13. Figure 16(b), shows a close-up of the hanging lamp sensor and its adjustable electrodes.

Data was taken for the target passing through a detection field 7.2 m long positioned symmetrically about the center of the lamp (along the black line on the floor in Figure 16(a)). This path was chosen to correspond to the simulated path described in Section V-D.

Exactly 37 data points were taken from each pass in the experimental setup in order to ease the comparison to the simulated data. At the sampling rate of 13.75 sps, 37 data samples took approximately 2 seconds. Some trial and error was necessary to acquire data that was situated symmetrically about the time axis in the resulting output plot. The experimental offset was measured as the value of the first data point taken from the sensor (corresponding to the case when the target is not well within the detection field). That offset was subtracted from all of the experimental data. Experimental setup parameters including passive component values for the sensor are summarized in Table VII.
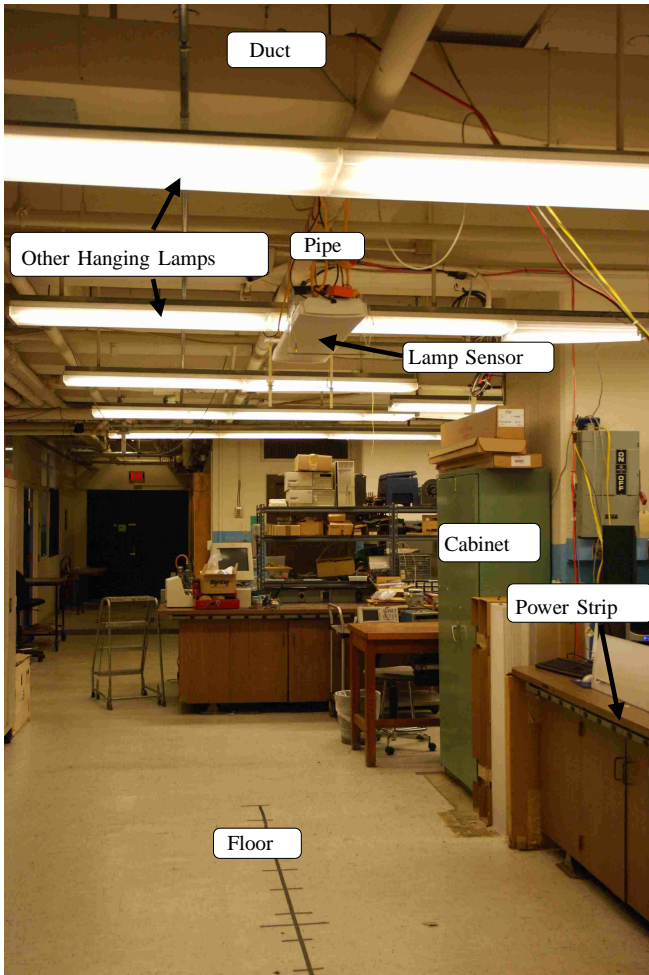
(a) A photograph of the experimental setup.
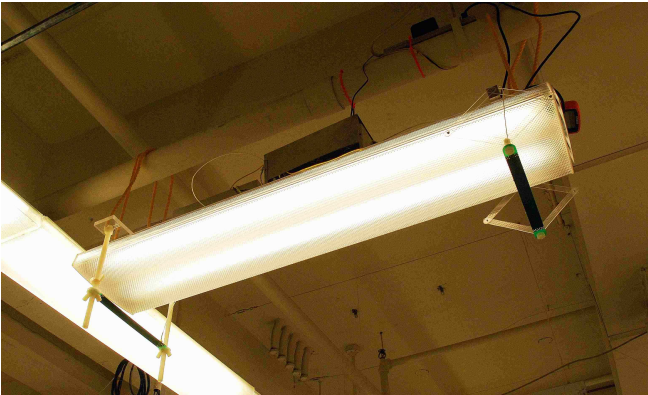
(b) A close-up photograph of the hanging lamp sensor.

Fig. 16: Photographs of the hanging lamp experimental setup.

F. Model Evaluation

Figure 17 shows three comparisons between measured data taken from the lamp sensor and simulated data taken from the circuit in Figure 18. The three plots in Figure 17 correspond to three different lamp heights, 2.28 m, 2.43 m and 2.58 m measured between the floor and the bottom of the bulb surfaces in the experimental setup. They show good agreement among the simulated and experimental data. Scripts for extracting data

TABLE VII: Experimental Setup Parameters.

Experimental Parameter	Note / Value
$R_{f1,2}$	10 MΩ
$C_{f1,2}$	7.5 pF
R_{f3}	200 kΩ
C_{f3}	660 pF
f_c	50 kHz
Phase Ref Elect.	Integrated as Trace in Ballast
Earth, gnd, Common	Explicitly connected
Electrode Depth	14.5 cm
Electrode Spacing	98 cm
Lamp Height	2.28, 2.43, 2.58 m
Target Height	1.83 m

from the SPICE .log files and generating the plots in Figure 17 can be found in reference [7].

The system model in this section was presented "as-is" with little or no simplification. That is, the intent was to include all of the capacitances between all of the conducting nodes in the system as a starting point for a working model. Undoubtedly, accurate prediction is possible without considering all of those capacitances. Moreover, the simulation likely discounts some capacitances that may influence the sensor response. Finally, the limitations of the lumped-element capacitive model described in Section II-D should be considered when evaluating the model presented here.

G. Effective Capacitive Sensitivity

From the lamp sensor response in Figure 17, and the simulated capacitances taken from FastCap®, the sensitivity of the lamp sensor to changes in capacitances (effective capacitive sensitivity) can be inferred. Table VIII, shows the capacitances that vary with the target for two different simulations. The first column shows capacitances for the target positioned 40 cm to the left of the left end of the lamp ($x = -100$ cm). The second column shows capacitances for the target positioned 20 cm to the left of the left end of the lamp ($x = -80$ cm). The third column shows the change in those capacitances. In the lampsensor output plot of Figure 17, this corresponds to a change of at least 10 mV. Compared to typical noise levels of about 200 μV, like those in Figure 10, a deviation of 10 mV is quite significant. Therefore, based on simulation and experiment, the lamp sensor appears to easily measure changes in the capacitances below the lamp on the order of 10's and 100's of fF.

TABLE VIII: Simulated Capacitance Change: $x = -100$ cm to $x = -80$ cm.

Capacitance	$x = -100$ cm	$x = -80$ cm	Change
L. Source-Target	214 fF	266 fF	52 fF
R. Source-Target	100 fF	133 fF	33 fF
L. Electrode-Target	394 fF	475 fF	81 fF
R. Electrode-Target	116 fF	144 fF	28 fF
Backplane-Target	13.2 pF	13.8 pF	600 fF
Cabinet-Target	3.6 pF	3.0 pF	600 fF

VI. CONCLUSION

A retrofit sensor system for fluorescent lamps was presented. A "balanced" measurement technique along with the use of

synchronous detection yielded a detection range of 10 ft. A lumped element capacitive model was presented and evaluated in simulation using Fastcap and SPICE. That simulation addressed the entire signal conditioning system including a circuit model of the front end amplifier. The resulting full-system model should be a useful starting point for further research and development.

Given a fluorescent lamp that can autonomously sense occupants, each lamp could be made to control its own brightness based on those measurements. Retrofitting a space or an entire building with such "auto-dimming" lamps would create an efficient and self-expanding autonomous energy management network. Moreover, implementing a cost-effective wireless link for communication between auto-dimming lamps would expand the possibilities for intelligent control of the lamps as well as other loads. Lighting would be controlled on as fine-grain a scale as is possible, virtually eliminating lighting of unoccupied spaces.

APPENDIX

A. FDA Model Netlist

```
.param ad = 2.794e6
.param ac = 8771.5
.param Zf = 423e3
.param ΔZf = 0.0
.param delZf = {ΔZf*Zf}
.param Zf1 = {Zf + 0.5*delZf}
.param Zf2 = {Zf − 0.5*delZf}
.param nomZf = {(Zf1+Zf2)/2}
.param Zind = {(2*nomZf/(1+ad))+(ac*delZf/(2*(1+ad)))}
.param Zinc = {0.5*nomZf}

R3FDA N001FDA edp {0.5*Zind}
R4FDA edm N002FDA {0.5*Zind}
R5FDA ecsource ec {Zinc}
Vpdummy + N001FDA 0
Vmdummy − N002FDA 0

Bedp edp ec V = 0.5*(i(vpdummy)+i(vmdummy))*(1/(1+{ad}))*(−0.5*{delZf}
−0.5*{nomZf}*{ac})
Bedm ec edm V = 0.5*(i(vpdummy)+i(vmdummy))*(1/(1+{ad}))*(−0.5*{delZf}
−0.5*{nomZf}*{ac})

Bec ecsource gnd V= −0.5*{delZf}*(i(vpdummy)−i(vmdummy))*0.5

Bvodp vopfda vocfda V = 0.5*(i(vpdummy)+i(vmdummy))*0.5*(−{ad}*{delZf}
+{ac}*{nomZf})/(1+{ad})+(i(vpdummy)−i(vmdummy))*0.5*(2*({ad}/(1+{ad})
)*{nomZf}−{ac}*{delZf}/(2*(1+{ad})))

Bvodm vocfda vomfda V = −0.5*(i(vpdummy)+i(vmdummy))*0.5*(−{ad}*{delZf}
+{ac}*{nomZf})/(1+{ad})+(i(vpdummy)−i(vmdummy))*0.5*(2*({ad}/(1+{ad}))
*{nomZf}−{ac}*{delZf}/(2*(1+{ad})))
Bvoc vocfda gnd V = {Vocm}
```

B. General SPICE Parameters

```
***General Parameters***
.param Vs = 200
.param fcarr = 50e3
.param stoptime = 10/{fcarr}

 ***Signal Source Model****
.param Vstrong = {Vs/2}
.param Vweak = {Vs/4}
.param Vend = {Vweak}
********************************
.param Vsupp = 6
.param RLP = 10
.param CLP = 1e−6
*********************Results********************
*************************************************
.measure Vout RESULT = avg(V(voutp,voutm)) from 150u to 200u
```

C. FastCap® Example list File (abridged)

`model.lst`

```
*G model.lst
*Syntax is "C objectfile.qui rel.perm xorigin yorigin zorigin"

*Group1
*Upper Left
C halfbulb.qui 1 0.007 0.0575 0
```

```
*Group2
*Lower Right
C halfbulb.qui 1 0.612 −0.0825 0

*Group3
*Lower Left
C halfbulb.qui 1 0.007 −0.0825 0

*Group4
*Upper Right
C halfbulb.qui 1 0.612 0.0575 0

*Group5
*Left Electrode .0762 = 3in. 0.1524 = 6 in.
C electrode.qui 1 0.12 −0.127 0.1524
*Group6
*Right Electrode
C electrode.qui 1 1.10 −0.127 0.1524

*Group7: Lamp Case and other conductors that will be earthed
C backplane.qui 1 0 −0.127 −0.07+
C sideplane.qui 1 −0.011 −0.127 −0.07+
C sideplane.qui 1 1.221 −0.127 −0.07+
C middlepart.qui 1 0.03 −0.05 −0.05+
C middlepart.qui 1 0.23 −0.05 −0.05+
C middlepart.qui 1 0.43 −0.05 −0.05+
C middlepart.qui 1 0.63 −0.05 −0.05+
C middlepart.qui 1 0.83 −0.05 −0.05+
C middlepart.qui 1 1.03 −0.05 −0.05+

C fixedlamps.qui 1 −0.47 −1 −0.22+
C fixedlamps.qui 1 1.85 −1 −0.22+
C powerstrip.qui 1 0 −1.2 1.5+
C pipe.qui 1 −2.5 −0.1 −0.45+
C duct.qui 1 1.25 −4.0 −1

*Group8
*Human Centered when x = 0.61−0.1 = 0.51
*C target.qui 1 0 0 1
C head.qui 1      −1.4      −0.050 0.625+
C torso.qui 1     −1.4      −0.225 0.90+
C legs.qui 1      −1.4      0.024 1.56+
C legs.qui 1      −1.4      −0.15 1.56

*Group9
*Unmovable floating conducting objects: "cabinet" for short
C cabinet.qui 1 −2.1 −1.7 0.4

*Group 10
*Floor or whatever is under the floor
C bigfloorpart.qui 1 −3.5 −0.5 2.48+
C bigfloorpart.qui 1 −3.5 0.0 2.48+
C bigfloorpart.qui 1 −3.0 −0.5 2.48+
C bigfloorpart.qui 1 −3.0 0.0 2.48+
```
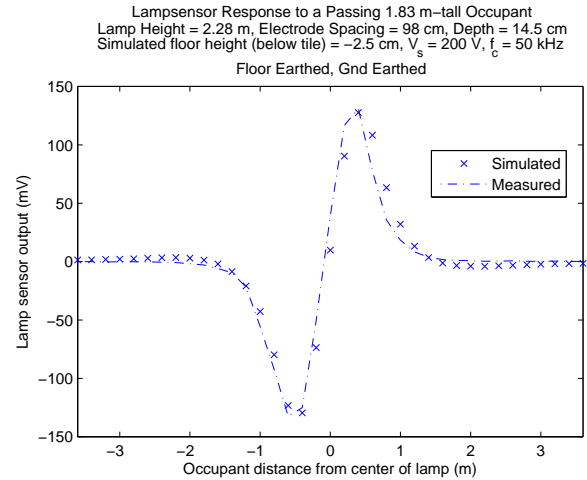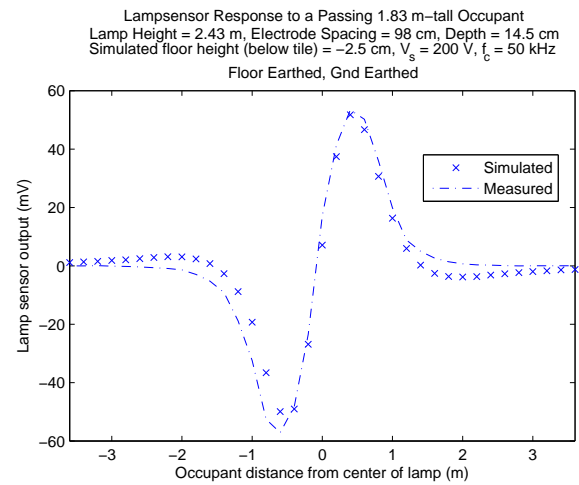
REFERENCES

[1] U. D. of Energy, "Annual energy outlook 2010 tables a4 and a5," Energy Information Administration, February 2010.

[2] J. J. Cooley, "Capacitive sensing with a fluorescent lamp," Master's thesis, Massachusetts Institute of Technology, 2007.

[3] J. Cooley, A.-T. Avestruz, and S. Leeb, "Proximity detection and ranging using a modified fluorescent lamp for security applications," in *Carnahan Conferences Security Technology, Proceedings 2006 40th Annual IEEE International*, oct. 2006, pp. 1 –8.

[4] ——, "A modified fluorescent lamp for discreet biometric surveillance," in *Technologies for Homeland Security, 2007 IEEE Conference on*, may 2007, pp. 227 –233.

[5] J. Cooley, A.-T. Avestruz, S. Leeb, and L. Norford, "A fluorescent lamp with integral proximity sensor for building energy management," in *Power Electronics Specialists Conference, 2007. PESC 2007. IEEE*, june 2007, pp. 1157 –1163.

[6] J. Cooley, A.-T. Avestruz, and S. Leeb, "An autonomous distributed demand-side energy management network using fluorescent lamp sensors," in *Power Electronics Specialists Conference, 2008. PESC 2008. IEEE*, june 2008, pp. 3907 –3916.

[7] J. J. Cooley, "Ph.d. thesis," 2010, massachusetts Institute of Technology.

[8] W. Buller and B. Wilson, "Measurement and modeling mutual capacitance of electrical wiring and humans," *Instrumentation and Measurement, IEEE Transactions on*, vol. 55, no. 5, pp. 1519 –1522, oct. 2006.

[9] J. Smith, "Field mice: Extracting hand geometry from electric field measurements," *IBM Systems Journal*, vol. 35, 1996.

[10] O. Fujiwara and T. Ikawa, "Numerical calculation of human-body capacitance by surface charge method," *Electronics and Communications in Japan*, vol. 85, no. 12, 2002.

[11] B. George, H. Zangl, T. Bretterklieber, and G. Brasseur, "A novel seat occupancy detection system based on capacitive sensing," in *Instrumentation and Measurement Technology Conference Proceedings, 2008. IMTC 2008. IEEE*, may 2008, pp. 1515 –1519.

[12] M. Tartagni and R. Guerrieri, "A fingerprint sensor based on the feedback capacitive sensing scheme," *Solid-State Circuits, IEEE Journal of*, vol. 33, no. 1, pp. 133 –142, jan 1998.

[13] H. Chu, J. Mills, and W. Cleghorn, "Design of a high sensitivity capacitive force sensor," in *Nanotechnology, 2007. IEEE-NANO 2007. 7th IEEE Conference on*, aug. 2007, pp. 29 –33.

[14] F. Han, Q. Wu, R. Zhang, and J. Dong, "Capacitive sensor interface for an electrostatically levitated micromotor," *Instrumentation and Measurement, IEEE Transactions on*, vol. 58, no. 10, pp. 3519 –3526, oct. 2009.

[15] A. Kuijpers, R. Wiegerink, G. Krijnen, T. Lammerink, and M. Elwenspoek, "Capacitive long-range position sensor for microactuators," in *Micro Electro Mechanical Systems, 2004. 17th IEEE International Conference on. (MEMS)*, 2004, pp. 544 – 547.

[16] S. Chatzandroulis, D. Tsoukalas, and P. Neukomm, "A miniature pressure system with a capacitive sensor and a passive telemetry link for use in implantable applications," *Microelectromechanical Systems, Journal of*, vol. 9, no. 1, pp. 18 –23, mar 2000.

[17] M. Dokmeci and K. Najafi, "A high-sensitivity polyimide capacitive relative humidity sensor for monitoring anodically bonded hermetic micropackages," *Microelectromechanical Systems, Journal of*, vol. 10, no. 2, pp. 197 –204, jun 2001.

[18] T. Fabian and G. Brasseur, "A robust capacitive angular speed sensor," *Instrumentation and Measurement, IEEE Transactions on*, vol. 47, no. 1, pp. 280 –284, feb 1998.

[19] E. Ghafar-Zadeh and M. Sawan, "A hybrid microfluidic/cmos capacitive sensor dedicated to lab-on-chip applications," *Biomedical Circuits and Systems, IEEE Transactions on*, vol. 1, no. 4, pp. 270 –277, dec. 2007.

[20] C. Merritt, H. Nagle, and E. Grant, "Textile-based capacitive sensors for respiration monitoring," *Sensors Journal, IEEE*, vol. 9, no. 1, pp. 71 –78, jan. 2009.

[21] A. Ueno, Y. Akabane, T. Kato, H. Hoshino, S. Kataoka, and Y. Ishiyama, "Capacitive sensing of electrocardiographic potential through cloth from the dorsal surface of the body in a supine position: A preliminary study," *Biomedical Engineering, IEEE Transactions on*, vol. 54, no. 4, pp. 759 –766, april 2007.

[22] Y.-J. Wen, J. Granderson, and A. Agogino, "Towards embedded wireless-networked intelligent daylighting systems for commercial buildings," in *Sensor Networks, Ubiquitous, and Trustworthy Computing, 2006. IEEE International Conference on*, vol. 1, june 2006, p. 6 pp.

[23] P. Zappi, E. Farella, and L. Benini, "Enhancing the spatial resolution of presence detection in a pir based wireless surveillance network," in *Advanced Video and Signal Based Surveillance, 2007. AVSS 2007. IEEE Conference on*, sept. 2007, pp. 295 –300.

[24] Z. Zhang, X. Gao, J. Biswas, and J. K. Wu, "Moving targets detection and localization in passive infrared sensor networks," in *Information Fusion, 2007 10th International Conference on*, july 2007, pp. 1 –6.

[25] H. H. Kim, K. N. Ha, S. Lee, and K. C. Lee, "Resident location-recognition algorithm using a bayesian classifier in the pir sensor-based indoor location-aware system," *Systems, Man, and Cybernetics, Part C: Applications and Reviews, IEEE Transactions on*, vol. 39, no. 2, pp. 240 –245, march 2009.

[26] E. Deng and S. Cuk, "Negative incremental impedance and stability of fluorescent lamps," in *Applied Power Electronics Conference and Exposition, 1997. APEC '97 Conference Proceedings 1997., Twelfth Annual*, vol. 2, feb 1997, pp. 1050 –1056 vol.2.

[27] J. J. Cooley, A.-T. Avestruz, and S. B. Leeb, "A design-oriented analytical approach for fully-differential closed-loop op-amp circuits," March 2010, submitted to IEEE Transactions on Circuits and Systems.

[28] A. D. Inc., "Ad8620 datasheet," 2008.

[29] T. I. Inc., "Ths4140 datasheet," 2004.

[30] J. K. Roberge, *Operational Amplifiers: Theory and Practice*. John Wiley and Sons, Inc., 1975.

[31] L. T. Corp., "Ltc2440 datasheet," 2002.

[32] K. Nabors and J. White, "Multipole-accelerated capacitance extraction algorithms for 3-d structures with multiple dielectrics," *Circuits and Systems I: Fundamental Theory and Applications, IEEE Transactions on*, vol. 39, no. 11, pp. 946 –954, nov 1992.
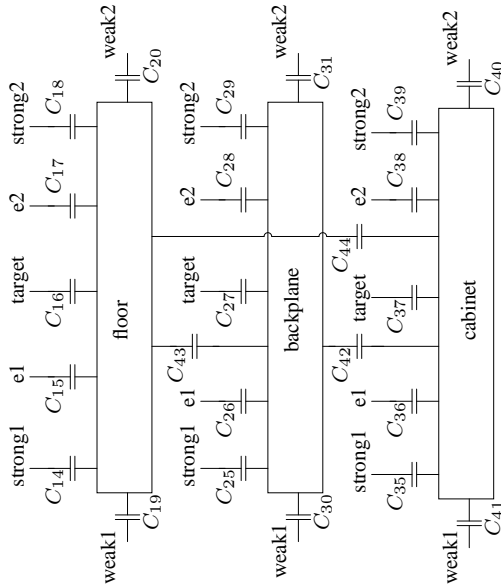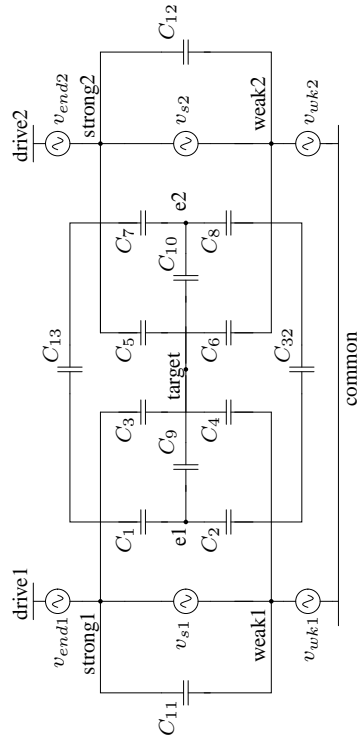
(a) Lamp Height = 2.28 m
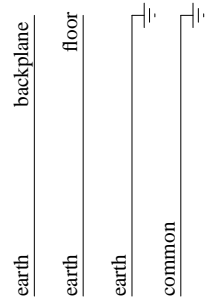

(b) Lamp Height = 2.43 m
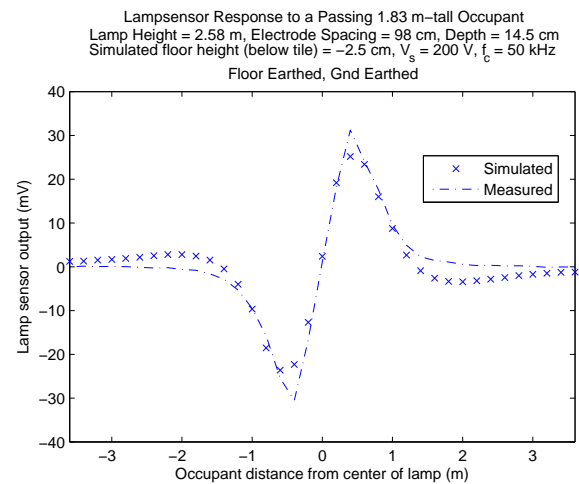
(c) Lamp Height = 2.58 m

Fig. 17: Plots of simulated and measured lamp sensor output data for various lamp heights.
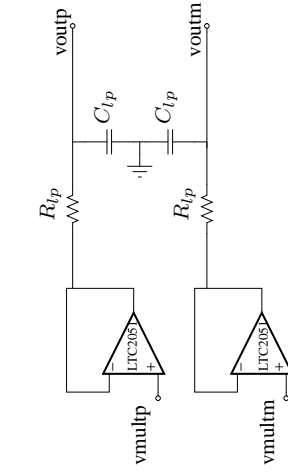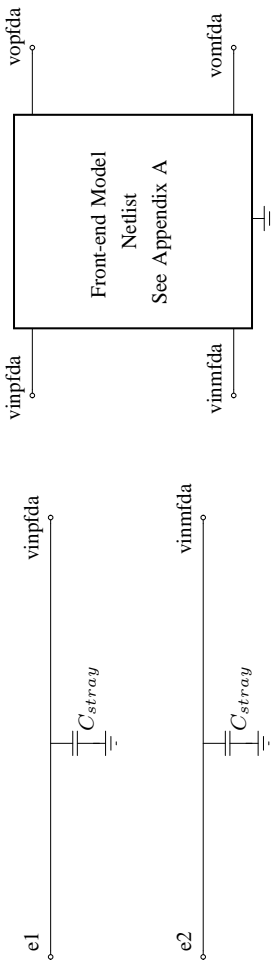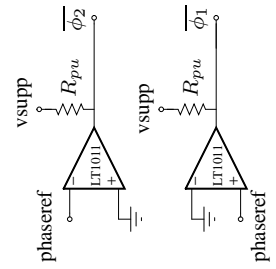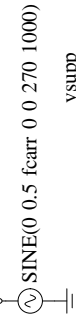
Fig. 18: A SPICE simulation of the capacitive model, FD transimpedance amplifier front end and the signal conditioning electronics.